Nanoscale

Accepted Manuscript

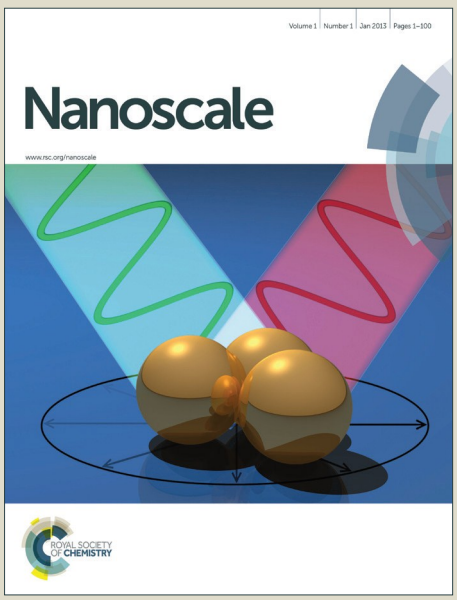

ROYAL SOCIETY OF CHEMISTRY

www.rsc.org/nanoscale

Journal Name

ARTICLE TYPE

Cite this: DOI: 10.1039/xxxxxxxxxx

Nanostructured SnS with Inherent Anisotropic Optical Properties for High Photoactivity†

Malkeshkumar Patel,*[ab‡] Arvind Chavda,[a] Indrajit Mukhopadhyay,[a] Joondong Kim,[b] and Abhijit Ray*[a]

Received Date
Accepted Date

DOI: 10.1039/xxxxxxxxxx

www.rsc.org/journalname

In view of the worldwide energy challenge in the 21st century, the technology of semiconductor-based photoelectrochemical (PEC) water splitting has received considerable attention as an alternative approach for solar energy harvesting and storage. Two-dimensional (2D) structures such as nanosheets have the potential to tap the solar energy by locking the functional properties at nanoscale. Tin (II) sulfide is a fascinating solar energy material due to its anisotropic material properties. In this manuscript, we report exploiting the 2D structure modulated optical properties of nanocrystalline SnS thin films synthesis by chemical spray pyrolysis using ambient transport in the harvesting of solar energy. We obtained the nanostructured SnS with well preserved dimensions and morphology with one step processing. The work demonstrates that the intrinsically ordered SnS nanostructure on FTO coated glass can tap the incident radiation using in an efficient manner. The structure-property relationship to explain the photo-response in nano-SnS is verified experimentally and theoretically. The novel design scheme for antireflection coating along with the anisotropic properties of SnS is conceived for realizing a PEC cell. The developed PEC cell consists of SnS photoanode shows considerably high photocurrent density of 7 mA cm^{-2} with aqueous media under AM 1.5G, 100 mW cm^{-2} exposure with notably stable operation. Electrochemical impedance spectroscopy revealed that a non-ideal capacitive behavior as well as drift assisted transport across the solid-state interface is responsible for such a high photo-current density in the nano-SnS photoanode.

1 Introduction

Sunlight could be the sole source of our future energy use, if the efficient and economical systems using earth abundant materials could be conceived for the energy conversion. Solar energy, for example can be converted into electricity and chemical fuels for the utilization and storage of energy. However, scientific challenges involved with this process include schemes to capture, convert, and store the energy. Solar energy conversion is of particular interest owing to the abundance of the source.[1–3] Nanostructures of earth abundant materials have an immense potential in unlocking their functional properties.[4,5] Two dimensional functional nanomaterials have received special attention in this reagrd.[6] Among the layered chalcogenide, tin monosulfide (SnS) is a promising earth abundant solar energy harvester due to the direct optical band gap of 1.4 eV with very high absorption coefficient[7–9] over the 5 × 10^4 cm^{-1}. SnS shows intrinsic p-type conductivity. However, its conductivity type can be modified by changing the Sn/S ratio. Ab-initio studies have shown that the Sn vacancies act as shallow acceptors, giving rise to a p-type conductivity, whereas the Sn on S antisites act as donor defects. Recently, high quality SnS monolayer has exhibited the n-type conductivity.[7] The homojunction solid state device fabricated from SnS material may avail the wireless water splitting due to exceptional accepter and donor doping possibility.[10,11] The orthorhombic layered structure of SnS composed of weakly interacting layers held together by van der Walls interactions, where each Sn and S atoms are tightly bound by chemical bonds with 100% exposed surface atoms (see Figure S1, Supplementary Information (SI)). Moreover, no surplus charge is present on the chemically stable surfaces of SnS monolayer.[7,12] SnS promotes fast separation efficiency of photogenerated electrons and holes because of its high mobility of 2.37 × 10^4 cm^2/V s and 7.35 × 10^4 cm^2/V s, respectively.[13] The recent experiment and theory suggest that

[a] Solar Research and Development Center, Pandit Deendayal Petroleum University, Gandhinagar 382007, Gujarat, India. Fax: 91 79 23275030; Tel: 91 79 23275304; E-mail: mpethani@gmail.com; abhijit.ray1974@gmail.com
[b] Photoelectric and Energy Device Application Lab (PEDAL), Department of Electrical Engineering, Incheon National University, 119 Academy Rd. Yeonsu Incheon, 406772, Korea.

† Electronic Supplementary Information (ESI) available: [details of any supplementary information available should be included here]. See DOI: 10.1039/b000000x/

‡ Present address.

α-SnS single crystal contains anisotropic electrical, optical and transport properties.[14,15]

In spite of highly functional material properties of layered SnS, their applications have been less explored, such as in photovoltaic cell,[8] photoelectrochemical cell,[7] batteries,[16,17] supercapacitors,[18–20] sensors,[21,22] solid state devices,[23–25] and field emission electrode.[26] A certified power conversion efficiency of 4.36% has been reported for substrate configured Mo/SnS/SnO_2/Zn(O,S)/ZnO/ITO solar cell device, where 400 nm thin SnS was deposited by atomic layer deposition.[8] However, the simplest atomic layer thin monolayer SnS electrode have exhibited power conversion efficiency of 3.32% with photocurrent density of 5.27 mA cm^{-2} for photoelectrochemical device for water splitting application with excellent stability.[7] SnS is stable in the presence of water and oxygen in the atmosphere , where it is found as natural mineral, Herzenbergite.[7,8] Hence, SnS has better prospects for long-term stability in aqueous electrolyte with anodic operation.[7] The SnS materials also enjoy the advantage of fabricating good quality thin films by nonvacuum processes.[7,27–29].

In this work, we have exploited the advantage of producing nanostructured SnS thin films by chemical spray pyrolysis where its structure could be well controlled from the precursor level that eventually have proved its potential as an efficient photoelectrode in the PEC cell. The self sustained nanostructure growth during the deposition process has been identified responsible for the functionality governed by the anisotropic optical properties for solar energy harvesting. A comprehensive, structural, physical, optical and electrical properties of the developed nanostructured α-SnS has been studied experimentally and interrelated with theory using first principle calculation. The optimally organized nanostructured SnS photoanode have exhibited a high photoactivity by delivering a high photocurrent density of 7 mA cm^{-2} with stable operation in the aqueous electrolyte. The results are compared with reported literatures in following discussion. The design scheme for the optimal thickness and orientation of anisotropic optical layers of α-SnS is presented in detail from the obtained quantitative measurements.

2 Experimental

2.1 Synthesis and deposition of nanostructured SnS thin films

Nanostructured SnS were synthesized and deposited by the chemical spray pyrolysis of aqueous solution of $SnCl_2{\cdot}2H_2O$ (SC) and thiourea (TU) on microscopic glass (15 mm $\times$ 50 mm) and F:SnO_2 (FTO) coated glass (15 mm $\times$ 50 mm, thickness 2.2 mm and of sheet resistance 15 Ω/square) as substrates. The concentration of SC and TU was maintained at 0.05M and 0.037M throughout the present study, respectively. We added 0.55-0.65 ml of HCl (35-38% LR, S D Fine Chem. Ltd.) to enhance the solubility of SC. All chemicals and substrates were procured from Sigma-Aldrich and used without any further purification otherwise it is mentioned. The pyrolysis temperature 375$\pm$10 °C was maintained for all the cases. The solution was transported to the spray nozzle using a syringe pusher and sprayed on the four step (dilute HCl, NaOH, DI water and Acetone) ultrasonically cleaned substrate at a flow rate of 1 ml min^{-1} for a duration of 3 minutes. Three to eight cycles of spray pyrolysis were carried out to obtain different thicknesses (50-500 nm). Ambient compressed air was used as the carrier gas at a pressure of 1.5 kg cm^{-2}. By controlling the exhaust fan the laminar flow of the nebulized precursor solution was achieved for the uniform deposition condition. The nozzle was scanned over the substrate geometry at the speed of 2 and 20 mm s^{-1} during the spray process in horizontal and vertical directions, respectively. The speed of exhaust fan increased at 5000 rpm for removal of the decomposed residual gases from the chamber to avoid the possible chemical reaction and contamination after the pyrolysis process for each cycle. Top view of the deposited nanostructured SnS thin films are shown in section S1 (SI). After the SnS deposition process, the substrate was naturally cooled down to 50 °C and then removed from the spray station. The deposited SnS films appeared to be dark red under daylight transmission.

2.2 Material characterization

The nanostructured SnS thin films were characterized by X-ray diffraction (XRD), Field emission scanning electron microscope (FESEM), Raman spectroscopy, Energy dispersive spectroscopy (EDS), Atomic force microscope (AFM), UV-visible diffuse reflectance spectroscopy (DRS) and Hall measurements. The XRD patterns were recorded by PANalytical X'Pert Powder diffractometer in the Gonio mode, using Cu-$K_{\alpha 1}$ radiation, (1.540598), with a step size of 0.05°, and time/step size = 0.5 s/step in the range of 2θ = 10-80° with thin film mode attachment. The planar and cross sectional morphology were analyzed by FESEM (Zeiss, Ultra 55) with 5 kV accelerating voltage using secondary emission (SE) detector at 10 mm of working distance. The thickness of all samples were determined from the cross sectional FESEM measurements. Raman spectroscopy (Micro Raman System, Jobin Yvon Horibra LABRAM-HR visible (400-1100 nm)) with an exciting wavelength of 480 nm was carried out to check for the phase purity and presence of any additional phases of tin sulfide. The surface area was investigated by an Atomic Force Microscopy (AFM) (AFM, Nanosurf AG). The elemental composition of the films was determined by energy dispersive spectroscopy (EDS) attached to the SEM with an accelerating voltage up to 20 kV. Optical characterization was carried out by a UV-visible diffuse reflectance spectrophotometer (Shimadzu, UV-2600) by recording the transmission and absorbance spectra of the films in the range of 320-1400 nm. The electrical properties were studied by Hall-measurement (Ecopia Corporation, HMS-5000) using Van der Pauw contact configuration with In contact.

2.3 Photoelectrochemical cell

The photoelectrochemical (PEC) measurements were carried out in a three electrode cell attached to a potentiostat galvanostat (CH Instruments, CHI 660D). The nanostructured SnS films deposited FTO glass, Pt foil and Ag/AgCl electrode were used as working, counter and reference electrodes, respectively. To see the effect of electrolyte on the PEC cell, the aqueous solution of

0.1M ($K_4Fe(CN)_6$) + 0.01M $K_3Fe(CN)_6$, and 0.1M $Na_2S_2O_3$ and 0.1M KOH were employed. AAA class solar simulator (Photo Emmision Tech Inc., model SS80) with 75 mm × 75 mm field aperture under AM1.5G (100 mW cm^{-2}) were used as light source. The light intensity was calibrated by the certified standard silicon reference cell. For routine testing of photoanode, a white high power LED (Wenrun,WR- 295 EC150150UW-1000C-9P40) excited (600 W m^{-2}) at 15.2 V DC with mechanical chopping at a frequency of 4 Hz was used. The LED source was calibrated with solar power meter (KUSAM-MECO, KM-SPM-11). A scan rate of 50 mV s^{-1} with sample interval of 0.1 mV was fixed during Linear Sweep Voltammetry (LSV) (scan direction was negative to positive potential in all cases). The Mott-Schottky analysis (Capacitance-Voltage (C-V) characteristics) of photoelectrodes were carried out at an AC amplitude of 0.5 mV and frequency of 1 kHz with sample interval of 0.05 V from reverse to forward bias scan direction in the DC bias range from -1.0 V to 0.6 V. The electrochemical impedance spectra (EIS) of the PEC cells were measured in a potentiostat/galvanostat attached with a frequency response analysis module. The EIS measurement for the developed PEC cells was carried out using an AC signal of amplitude 5 mV in the frequency range from 1 Hz to 1 MHz superimposed by a DC bias of from 0.05 to 0.5 V under actual dark conditions. The stability study (photo corrosion) was performed in bulk electrolysis mode with coulometry at an applied potential less than the on-set for 0.1M ($K_4Fe(CN)_6$) + 0.01M $K_3Fe(CN)_6$ electrolyte with SnS photoathode for 200 s to 2 hr. All the PEC measurements were performed under physically uninterrupted (no stirring, Ar or N_2 bubbling or ultrasonication) environment. All measurements were performed at room temperature.

3 Results and Discussion

Fig. 1a represents the XRD pattern of the nanostructured SnS deposited on the FTO coated glass substrate. The SnS material was considered to have orthorhombic crystal symmetry with space groups of *Pbnm* (62) according to COD-AMSCD 9008785. The structural parameters derived for the α-SnS are shown in the Section S2 (SI). The background of the FTO reflection are masked with recorded background XRD spectra (Figure S2). The structural and morphological properties of the employed FTO substrate are shown in section S3 (SI). The distinct peak at 2θ = 32° suggests that the film contain a crystallographic texture in the (004) orientation which is dominant. This indicates that majority of its grains with total calculated exposed area of 52% were parallel to the substrate. As noted by Stevanovic et al. [14] it is equivalent to the orientation (100) according to the theory. The next dominant facets corresponding to 2θ = 31.54° were (111) with area coverage of 26%. Above results agree well with previous report of polycrystalline SnS film grown on glass substrates. [14] The room temperature Raman spectra as shown in Fig. 1b demonstrates four peaks at 91, 161, 185, and 218 cm^{-1} which correspond to one A_g, one B_{3g} (LO) and two A_g (LO), modes respectively. It closely matches with the Raman spectra reported for single crystal SnS. [7,16,30,31] It may be noted that, neither major A_{1g} mode (315 cm^{-1}) for SnS_2, nor that of Sn_2S_3 (153 cm^{-1}) or SnO_2 (472 cm^{-1}) were visible in the spectrum. It reveals the phase purity of the spray deposited α-SnS, while no impurities, such as SnS_2, Sn_2S_3 and SnO_2 were present. [16,30,32] The surface morphology as seen from the FE-SEM images taken at different magnifications, is shown in Fig. 1c. Low magnification image shows that the film was uniform and defect free. Higher magnification images reveal the formation of randomly oriented slightly vertical petal-like SnS nanostructure on the FTO substrate with higher surface to volume ratio. For the understanding the growth of nanostructured α-SnS, the cross section of different layer thickness are shown in Fig. 1d. Initially an uniform few layered SnS was formed during the pyrolysis process on the FTO surface, later the surface energy changes dynamically and the growth becomes random and the layers of the SnS materials start the growth along the direction of spray. The average length of the petal kind microstructure was measured to be 280 nm in the the inclined horizontal direction. The obtained microstructure is in agreement with that reported in SnS films synthesized using the vacuum techniques, such as atomic layer deposition [30], thermal evaporation [33], pulsed laser deposition [34] and sputtering [35]. It is interesting to note that the surface morphology as observed is highly beneficial for photoelectrchemical reaction due to its high aspect ratio or surfacial length. A qualitative assessment of the surfacial length can be made through AFM as shown in Section S4 (SI). The surfacial length of α-SnS may be controlled by varying the thickness from 100 to 500 nm. The maximum surfacial length ratio 2.5 is possible for α-SnS with thickness of 450 nm.

Fig. 2 shows the optical properties of the nanostructured α-SnS film on the FTO substrate. The absorbance, transmittance and reflectance are shown in Fig. 2a. A 210 nm thick SnS film exhibited excellent absorption characteristic with minimum reflectance in the visible range. The absorption coefficient (α) of the films was estimate by the relation,

$$\alpha = \frac{1}{d} ln\left(\frac{(1-R)^2}{T}\right), \quad (1)$$

where, d, R and T are the thickness, reflectance and transmittance of the SnS film. The absorption coefficient α calculated for the developed nanostructured SnS was found to be in the range 3.9 × 10^4 to 2.7 × 10^5 cm^{-1} for the visible range of solar spectrum from 700 to 390 nm. Therefore, the 256 nm thick nanostructures of SnS film can absorb the maximum of the visible solar irradiation. The α at the energy band gap and peak wavelength of AM 1.5G spectrum is highlighted in Fig. 2b. However, 60 nm thick nanostructures of SnS film is sufficient to absorb the maximum spectrum density of incidental solar irradiation, which is illuminated at the wavelength of 530 nm. The bandgap, E_g of the SnS film was estimated by the Tauc plot as well as by derivative are shown in Fig. 2c, where h and ν is the Planck's constant and the photon frequency, respectively. It have confirmed the direct E_g = 1.42-1.44 eV. [27,36]

In addition, Tauc plot of the Kubelka-Munk function was applied to estimate both direct and indirect band gap transitions of nanoscaled SnS films. According to the Kubelka-Munk function relation,

$$F(R) = \frac{\alpha}{S} = \frac{(1-R_\infty)^2}{2R_\infty}, \quad (2)$$

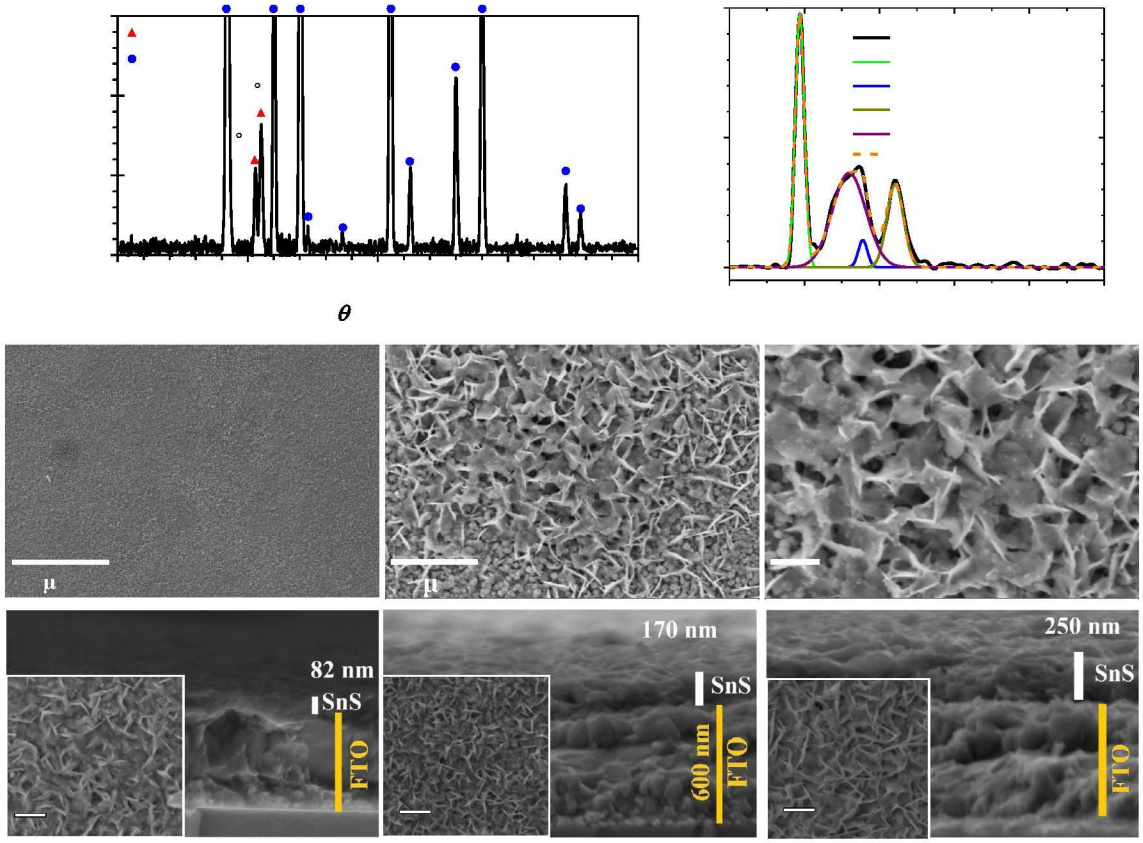

Fig. 1 (a) X-ray diffraction pattern, (b) Raman spectra, (c) FESEM images of topography at different magnification and (d) Cross sectional view of SnS thin films of various thicknesses on FTO coated glass substrate (Corresponding topography of SnS layer are shown in inset). All samples were prepared under identical conditions as mentioned in section 2.1 (experimental).

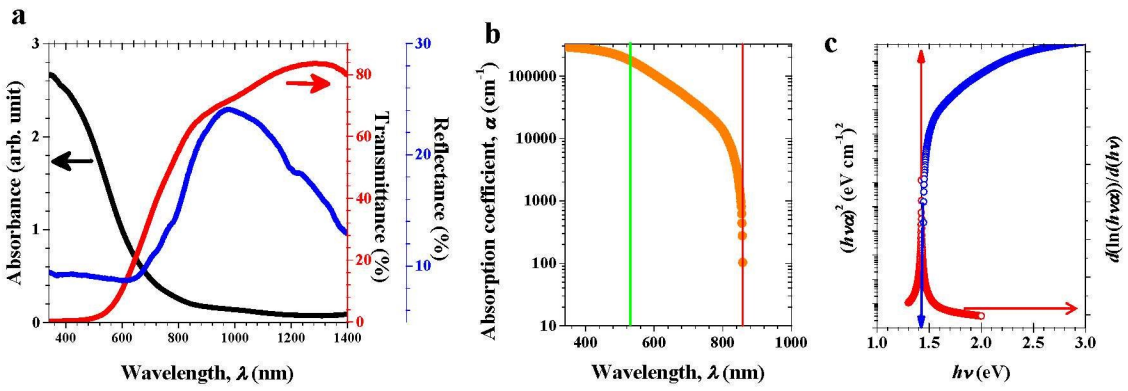

Fig. 2 Optical properties of nanostructured SnS thin films. (a) Absorbance, transmittance and reflectance spectra, (b) absorption coefficient, α (c) Tauc plot and derivative of $ln(\alpha h\nu)$ vs. $h\nu$.

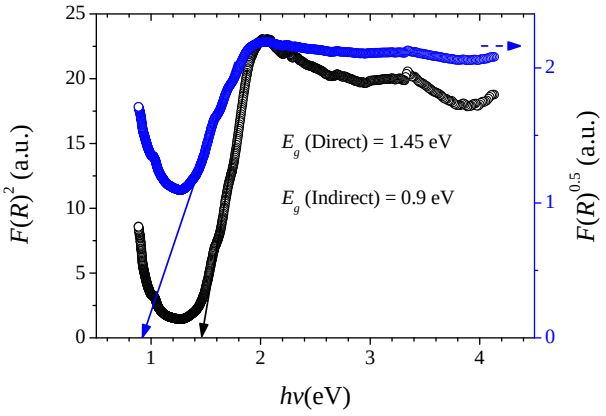

Fig. 3 A Tauc plot of the Kubelka-Munk function for direct and indirect allowed transitions.

The Kubelka-Munk function $F(R_\infty)$ is directly proportional to the absorption coefficient, and inversely proportional to scattering coefficient (S), where R_∞ is the diffused reflectance of the film.[28,29] The obtained results are shown in Fig. 3, revealed the direct and indirect bandgap transitions at 1.45 eV and 0.9 eV, respectively.

The UV-Visible diffused reflectance spectroscopy (DRS) exhibits resultant optical properties of the mixed orientation of the nanostructured α-SnS. Moreover, Banai *et al.* and Stevanovic *et al.* studied the optical properties and absolute band edge energies on the surface orientation of single crystal α-SnS using the density functional theory (DFT) for all surfaces, respectively.[14,15] Both the properties were found to be anisotropic. The anisotropic optical properties are important for estimating the optimum thickness of the α-SnS layers for minimal reflectance from the surface.[37–39] In order to develop a fundamental understanding on the energy band diagram, density of states of our nanostructured SnS, abinitio approach was adopted and implemented for the α-SnS (The structural presentation of super cell of α-SnS (*Pbnm*(62) in various lattice direction is shown in section S2).[7,14,15,40] The electronic structure of SnS was calculated within DFT using a screen exchange-correlation generalized gradient approximation functional developed by Armiento and Mattsson (GGA-AM05).[41] All calculations were performed using the Vienna Ab-initio Simulation Package (VASP) code,[42] with the projector augmented wave (PAW) approach,[43] a 258.7 eV default plane wave cut-off, and reciprocal space sampling of $6 \times 6 \times 4$ κ-point. Fig. 4a and b show the calculated electronic band structures and density of state. A direct optical band gap of 1.45 eV was evident at Γ symmetry point. This value is very close to that determined by Tauc plot and method of derivative (Fig. 2c,d, respectively). Our calculation also exhibited an indirect band gap of 0.9 eV, which follows an allowed transition.[44] However, the anisotropic nature of the band-structure, cause an optical transition at some higher photon energies, close to 1.4 eV.[30] The obtained energy band diagram and density of states closely match with previous reports.[7,15] It is noteworthy that as the density of state is higher near the valence band edge, it improves the carrier (photogenerated holes) transport efficiency.[7] Furthermore, Fig. 4c-e revealed the anisotropic nature of optical constants such as dielectric constant (ε_r), refractive index (n) and extinction co-efficient (κ). In general a combination of the anisotropic refractive index helps us to understand the measured resultant reflectance spectra. It shows an excellent agreement between the experiment (spectroscopy ellipsometry) and theory implemented for estimating the anisotropic optical constant.[15] Furthermore, the estimated optical constants were deployed for understanding the resultant reflectance and required optimum thickness of α-SnS top layer for minimal reflectance for the photoelectrochemical cells (PEC) as described in the following discussion.

The Mott-Schottky (MS) measurement was performed for the batch of α-SnS photoelectrode with various thickness from 40-500 nm on the FTO coated glass substrate. The technique is detailed in the section S5 (SI). The MS analysis allows us to make an accurate estimation of the flat band potential for given electrolyte, carrier concentration and types of majority carrier. All photoelectrode exhibited the positive slope of $d(C^{-2})/dV$, which confirms that all the SnS electrodes have n-type conductively with electron as majority carrier. However, stoichiometric SnS is expected to exhibit p-type conductivity due to intrinsic Sn-vacancy. The $1/C^2$ vs applied potential (V vs. Ag/AgCl) is shown in Fig. 5a. The SnS electrode have exhibited reasonable capacitance in the rage of μF for the given dark condition. It favors the formation of the strong depletion region inside the SnS layer with respect to reference electrode. The flat band potential, V_{FB} = -0.49 eV was estimated with 0.1M $K_4Fe(CN)_6$ electrolyte. The donor concentration, N_D of the photoanode SnS was calculated using following relation,[45]

$$N_D = \frac{2}{\varepsilon_0 \varepsilon_r q A^2} \left(\frac{d(C^{-2})}{dV} \right)^{-1}, \qquad (3)$$

The N_D value of 1.25×10^{15} cm^{-3} was estimated for the α-SnS photoanode. Therefore, the estimate values for the ΔE_F, electron affinity (χ) and workfunction (ϕ) were 0.2, 4 and 4.2 eV, respectively. The estimated electrical parameters of SnS photoanode carries great significance for developing the knowledge of charge transport and space charge width useful for the PEC applications. The calculated energy band diagram is shown in the Fig. 5b. The developed space charge width in the SnS photoelectrode for given potential vs. Ag/AgCl reference electrode is shown in Fig. 5c. A drift assisted transport in the space charge region at the lower potentials in the nanostructued SnS layer is evident from this analysis, which helps enhance the collection efficiency of the photogenerated carriers. The reproducibility of the MS analysis were checked for a number of SnS electrodes and analyzed, which are shown in the section S7 (SI). It shows N_D varies from 10^{14} to 8×10^{15} cm^{-3} for produced batch of SnS electrodes. A similar result was obtained for the atomically thin SnS layer with n-type conductivity with the N_D value[7] of 6.7×10^{16} cm^{-3}.

The photoresponse spectrum of the PEC cell under chopped white light illumination is shown in Fig. 6a. The onset potential (V_{on}) of the cell was found to be 0.25 V vs. Ag/AgCl. The region below the flat band can be directly assigned to the accumulation of majority carriers on the electrolyte side and hence a cathodic photocurrent is possible in the n-type semiconductor.

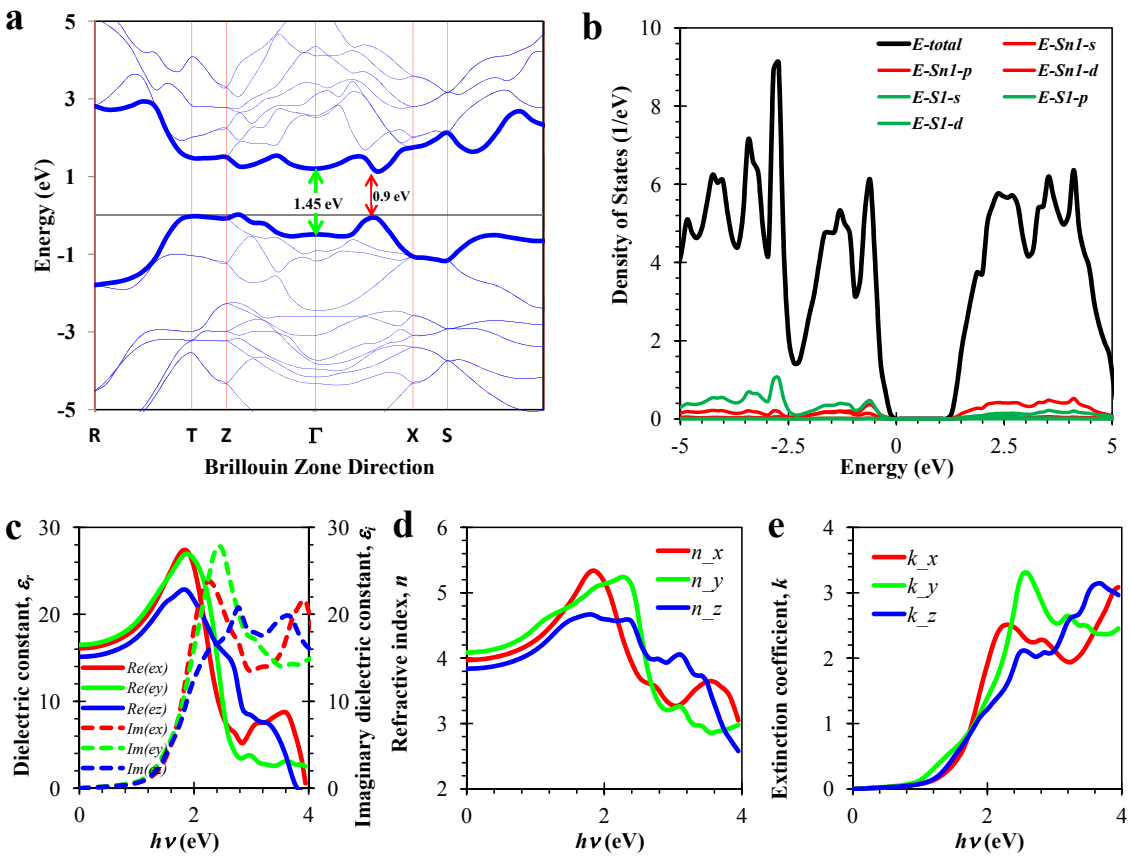

Fig. 4 (a) Calculated band structure of SnS supercell with direct bandgap of 1.45 eV and in-direct bandgap of 0.9 eV, (b) density of states, (c) dielectric constant, ε_r (d) refractive index, n and (e) extinction coefficient, k_r in x, y and z lattice directions.

The region just above the flat band is the depletion region as the band starts to align in response to the applied potential. A logarithmic increase in the photocurrent up to an applied potential of 0.9 V vs Ag/AgCl is found highest among those reported till date. A further increase in the applied potential up to 1.3 V causes a linear increase in the dark as well as photocurrent due to the depletion in the inversion region. The solar to chemical conversion efficiency of 4.7% was estimated at an applied potential of 0.7 V vs. Ag/AgCl (section S6 (SI)). The nanostructured SnS photoelectrode with significantly higher photocurrent densities as compared to other SnS photoelectrode systems previously reported in the literature are compared and listed in Table 1. Recorded photocurrent is several times higher than the previously reported SnS systems.[27,36,46] This work demonstrates the effectiveness of optically anisotropic and nanostructured SnS absorber that also works as antireflecting surfaces to further enhance photoelectrochemical cell efficiency.

Fig. 6b shows the energy diagram of the developed PEC cell using the SnS anode and Pt cathode, where the relative position of SnS band edges and the redox levels of the electrolyte is shown. The photogenerated holes leaving the SnS valence band are accepted by electrolyte and the oxygen evolution reaction occurs at the photoanode surface. On the other hand, photogenerated electron leave the conduction band to reach the Pt-counter electrode through the external wire and the hydrogen evolution reaction occurs at the Pt surface. The visual evidence of the evolved oxygen and hydrogen gases on the SnS and Pt surfaces, respectively is shown in Fig. 6cc. The oxygen and hydrogen evolution reactions (oxidation and reduction) are shown therein.

The electrochemical impedance spectroscopy is an important tool to understand the nature and quality of semiconductor/electrolyte interface and the associated time constant of charge transfer that governs the PEC cell efficiency. The Electrochemical impedance spectroscopy data of nanostructured SnS photoanode were analyzed based on the equivalent circuit models, as shown in Fig. 7. In the equivalent circuit, R_S, R_J and R_C are the series resistance of the cell, recombination resistance and charge transfer resistance at the pore electrolyte interface, respectively. The impedance data of nano-SnS photoanode was best described by introducing constant phase elements, instead of capacitances. Here, CPE-I (Q_J) and CPE-II (Q_C) are the constant phase elements related to the SnS/electrolyte interface including the double layer and capacitances of the pore electrolyte interface, respectively. The CPE impedances i.e., Z_{CPE} defined by their respective CPE exponents and frequency independent constant as follows:

$$Z_{CPE} = \frac{1}{(j\omega)^n Q}, \quad (4)$$

where, Q is the capacitance and the exponent n is 1 for an ideal capacitor. The chemical capacitance is expected to occur at the interfaces, where the density of states on each side differs to a great extent. For the PEC cell under investigation, the aqueous electrolyte has an infinite density of states relative to the semiconductor film, which leads to a chemical capacitance in addition to the double layer capacitance. Fitting the equivalent circuit to all the experimentally obtained impedance spectra at different

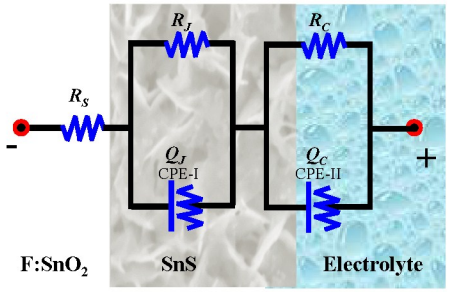

Fig. 7 Proposed equivalent circuit model of the PEC cell for electrochemical impedance spectroscopy.

applied potentials leads to the estimation of R_S, R_J, R_C,CPE-I and CPE-II.[47,48] Fig. 8a-c shows the set of Nyquist, bode amplitude and phase plots for constructed PEC cell, respectively. It is noteworthy that the applied potential higher than 0.4 V vs. Ag/AgCl exhibited the CPE near to the ideal capacitance. It apparently attributes to an ideal depletion region and improved collections of the photogenerated carries. The fitting parameters in each case are summarized in the Table 2. The fitting parameters provided an insight of the charge transport across the nano-SnS photoanode. As a result of the applied potential, the R_S is decreased from 53 to 25.4 Ω. The CPE exponent is found to be more ideal for an applied potential of 0.4 and 0.5 V, that signifies the formation of a nearly ideal junction. The junction's ideality is because of favorable depletion of strongly polarized free charge carrier in the SnS film. This facilitates the drift assisted transport of the photogenerated charge carries across the junction. Moreover, the CPE-II element remains less affected by the applied potential. The time constant calculated by the product of RC was an overall estimate without trying to separate the recombination and diffusion capacitances. Therefore, $t_j = R_J C_J$ and $t_c = R_C C_{bc}$ will be simply referred to the overall time constants of the junction and the contacts, respectively.[47,49–51] The magnitude of the circuit time constants represents the mean relaxation time of the respective interfaces. The time constant of the charge relaxation at the junction decreases from 5.5 ms to 1.75 ms for the applied potential V_{App} from 0.05 V to 0.5 V vs. Ag/AgCl. However, t_c remained unaffected in all the cases. The semicircular nature of Nyquist plot of the PEC cell indicates the stability of the photoelectrode under the larger applied bias. It shows the great level of stability without any chemical degradation for a longer duration.

Furthermore, to bring more understanding on the obtained larger photocurrent density, the multilayer antireflection coating for the constructed PEC cell was adopted. As SnS avail the anisotropic optical properties that facilitates various possible combinations of SnS layers on the FTO coated glass. In the case of PEC cell, the media for the light remains the aqueous electrolyte. The model formulation for the resultant surface reflectance from the combinations of the electrolyte, SnS layers and FTO is presented in section S8. The refractive index of the FTO and electrolytes are shown therein. For various cases the calculated reflectance was compared with the measured reflectance from the

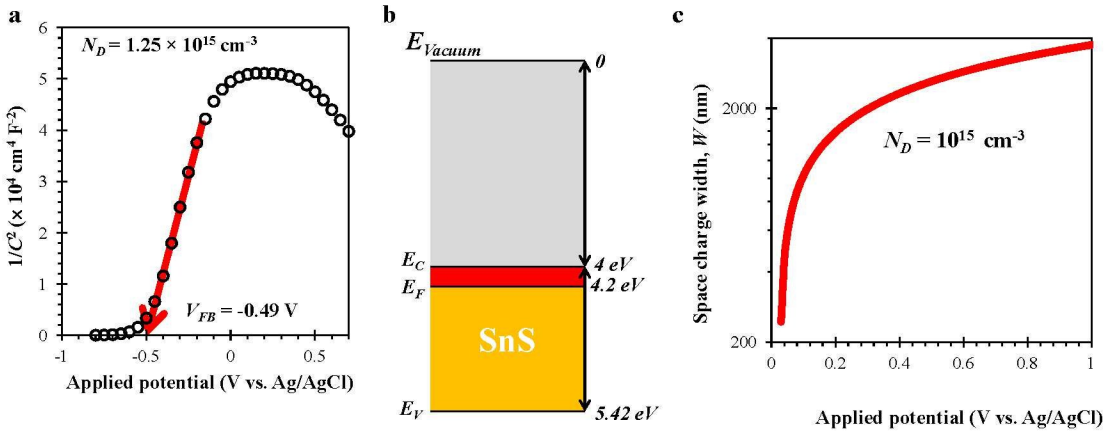

Fig. 5 (a) Mott-Schottky plot for the nanostructured SnS based photoelectrode measured at a frequency of 1 *k*Hz in the dark, (b) Estimated band edges and (c) Space charge width as a function of applied potential.

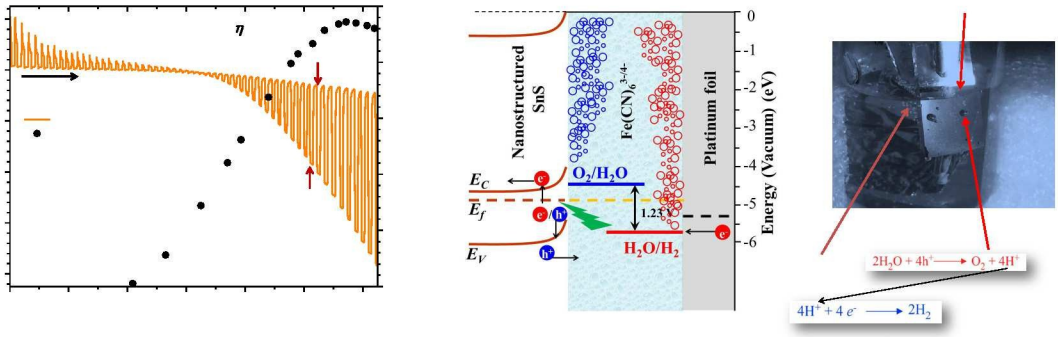

Fig. 6 Linear sweep voltammogram under chopped illumination, (b) the position of conduction and valence band of SnS relative to the water oxidation and the water reduction potential, and (c) digital photograph showing the constructed PEC cell with integrated SnS film with water splitting phenomena.

SnS surface. It provides an insight of the growth process of the SnS structures from one orientation to another. The best possible configuration is shown in the Fig. 9, where the various thicknesses of SnS-z orientation is varied as an optimization. The 50 nm thick SnS layer orientated in the z direction on the planar SnS layer provides a minimal reflectance through the nanostructured front surface leading to a highest absorption. The adopted approach is worth for other anisotropic two dimensional semiconducting materials for designing the optimum geometry and configurations. The record photocurrent density may attributed to the reduced reflectance from the semiconductor electrolyte interface. A cartoon of the integrated SnS film PEC cell is shown in the Figure S13 of SI to manifest the configuration that finally obtained the highest photocurrent density ever reported for the SnS film system.

4 Conclusions

In summary, we have developed high quality SnS material and its nanostructure for possible integration of anisotropic optical and transport properties for application in photoelectrochemical cell. The thin film exhibited a direct optical band gap of 1.42 eV with high optical absorption coefficient up to 2.7×10^5 cm^{-1} in the visible range of solar spectrum. The fabricated photoanode had a favorable donor concentration of 10^{15} cm^{-3} with the flat band potential of -0.49 V vs. Ag/AgCl as confirmed by Mott-Schottky measurement. The fabricated device was characterized to have an enhanced absorption controlled by the thickness of deposited layers. It may be attributed to an integrated anisotropic optical property of nanostructured α-SnS for which the reflectance is below 5% in the visible spectrum. The optimized device showed the highest photocurrent density of 7 mA cm^{-2} at an applied potential of 0.8 V vs. Ag/AgCl, making the nanostructured α-SnS a superior candidate for water splitting applications.

Acknowledgements

The authors thank the Solar Research and Development Center (SRDC, PDPU) for providing XRD and FE-SEM facilities. Defence Research and Development Organization (DRDO), New Delhi is being acknowledged for the use of Solar Simulator under Project No. ERIP/ER/1103946/M/01/ 1349. The authors acknowledge the financial support of the Korea Institute of Energy Technology Evaluation and Planning, in a grant funded by the Ministry of Knowledge Economy (KETEP-20133030011000). The Center for INU research facility is acknowledged for providing support of Raman spectroscopy measurements. Department of Science and Technology (DST), New Delhi is acknowledged for the potentiostat-galvanostat facility under Project No. SR/S1/PC-44/2011. Authors are grateful to Dr. U. Joshi at Department of Physics, Gujarat University for providing AFM facility.

References

1 H.-J. Lewerenz and L. Peter, *Photoelectrochemical Water Splitting: Materials, Processes and Architectures*, Royal Society of Chemistry, 2013.

2 N. S. Lewis and D. G. Nocera, *Proc. Natl. Acad. Sci. U.S.A.*, 2006, **103**, 15729–15735.

3 S. Hu, M. R. Shaner, J. A. Beardslee, M. Lichterman, B. S. Brunschwig and N. S. Lewis, *Science*, 2014, **344**, 1005–1009.

4 Q. Zhang, E. Uchaker, S. L. Candelaria and G. Cao, *Chem. Soc. Rev.*, 2013, **42**, 3127–3171.

5 T. Unold and H. Schock, *Annu. Rev. Mater. Res.*, 2011, **41**, 297–321.

6 S. Z. Butler, S. M. Hollen, L. Cao, Y. Cui, J. A. Gupta, H. R. Gutierrez, T. F. Heinz, S. S. Hong, J. Huang, A. F. Ismach *et al.*, *ACS Nano*, 2013, **7**, 2898–2926.

7 Y. Sun, Z. Sun, S. Gao, H. Cheng, Q. Liu, F. Lei, S. Wei and Y. Xie, *Adv. Energy Mater.*, 2014, **4**, 1300611.

8 P. Sinsermsuksakul, L. Sun, S. W. Lee, H. H. Park, S. B. Kim, C. Yang and R. G. Gordon, *Adv. Energy Mater.*, 2014, **4**, 1400496.

9 X. Rui, H. Tan and Q. Yan, *Nanoscale*, 2014, **6**, 9889–9924.

10 S. Y. Reece, J. A. Hamel, K. Sung, T. D. Jarvi, A. J. Esswein, J. J. Pijpers and D. G. Nocera, *Science*, 2011, **334**, 645–648.

11 G. Yue, Y. Lin, X. Wen, L. Wang and D. Peng, *J. Mater. Chem.*, 2012, **22**, 16437–16441.

12 W. Wang, K. Leung, W. Fong, S. Wang, Y. Hui, S. Lau, Z. Chen, L. Shi, C. Cao and C. Surya, *J. Appl. Phys.*, 2012, **111**, 093520.

13 M. Nassary, *J. Alloys Compd.*, 2005, **398**, 21–25.

14 V. Stevanović, K. Hartman, R. Jaramillo, S. Ramanathan, T. Buonassisi and P. Graf, *Appl. Phys. Lett.*, 2014, **104**, 211603.

15 R. Banai, L. Burton, S. Choi, F. Hofherr, T. Sorgenfrei, A. Walsh, B. To, A. Cröll and J. Brownson, *J. Appl. Phys.*, 2014, **116**, 013511.

16 A. M. Tripathi and S. Mitra, *RSC Adv.*, 2014, **4**, 10358–10366.

17 Y. Zhang, J. Lu, S. Shen, H. Xu and Q. Wang, *Chem. Commun.*, 2011, **47**, 5226–5228.

18 M. Jayalakshmi, M. M. Rao and B. Choudary, *Electrochem. Commun.*, 2004, **6**, 1119–1122.

19 J. Cai, Z. Li and P. K. Shen, *ACS Appl. Mater. Interfaces*, 2012, **4**, 4093–4098.

20 H. Chauhan, M. K. Singh, S. Hashmi and S. Deka, *RSC Adv.*, 2015, **5**, 17228–17235.

21 F. Lu, J. Yang, R. Li, N. Huo, Y. Li, Z. Wei and J. Li, *J. Mater. Chem. C*, 2014, **3**, 1397–1402.

22 M. Roosta, M. Ghaedi, A. Daneshfar, R. Sahraei and A. Asghari, *J. Ind. Eng. Chem.*, 2015, **21**, 459–469.

23 A. Umar, M. Akhtar, R. Badran, M. Abaker, S. Kim, A. Al-Hajry and S. Baskoutas, *Appl. Phys. Lett.*, 2013, **103**, 101602.

24 C.-H. Ruan, Y.-J. Lin, Y.-H. Chen and H.-C. Chang, *Mater. Sci. Semicond. Process.*, 2015, **32**, 62–67.

25 X. Guo, H.-J. Xie, J.-W. Zheng, H. Xu, Q.-K. Wang, Y.-Q. Li, S.-T. Lee and J.-X. Tang, *Nanoscale*, 2014, **7**, 867–871.

26 S. R. Suryawanshi, S. S. Warule, S. S. Patil, K. R. Patil and M. A. More, *ACS Appl. Mater. Interfaces*, 2014, **6**, 2018–2025.

27 M. Patel and A. Ray, *RSC Adv.*, 2014, **4**, 39343–39350.

28 S. M. Herron, J. T. Tanskanen, K. E. Roelofs and S. F. Bent, *Chem. Mater.*, 2014, **26**, 7106–7113.

29 P. D. Antunez, D. A. Torelli, F. Yang, F. A. Rabuffetti, N. S.

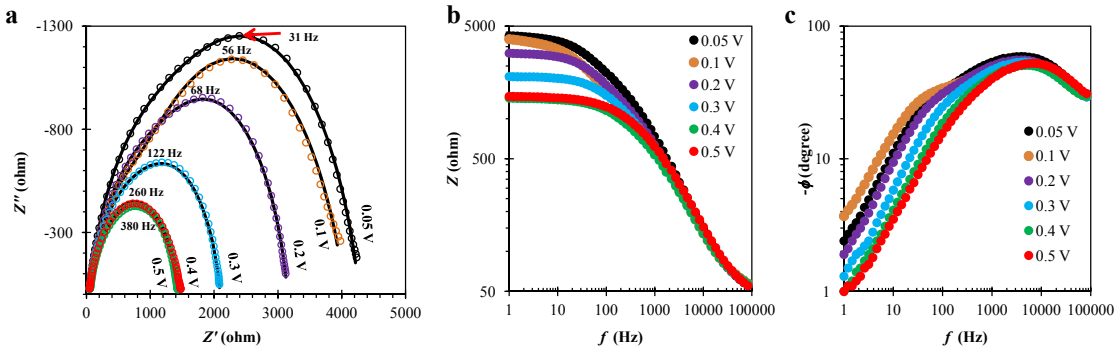

Fig. 8 Electrochemical impedance spectra for the nanostructured SnS photoelectrode at applied potential 0.05 - 0.5 V vs. Ag/AgCl under dark condition at room temperature (a) Nyquist plot, Z' and Z'' are the real and imaginary parts of impedance, respectively while the solid lines were fitted by EIS Spectrum Analyser software using the equivalent circuit as shown in Fig. 7, (b) Bode modulus and (c) Bode phase plots.

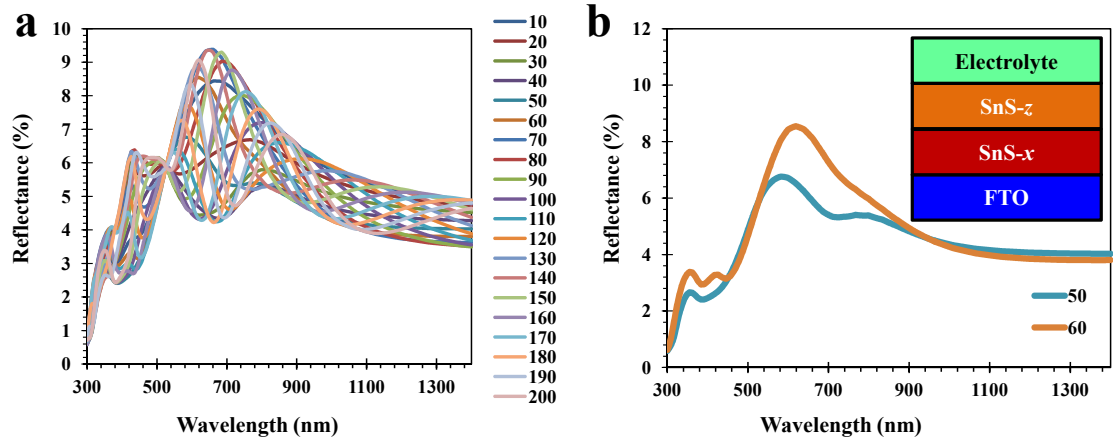

Fig. 9 The effect of thickness of preferred oriented nanostructure of SnS material on the total reflectance from the front surface of SnS, where the electrolyte considered as surrounding media. (a) effect of front layer thickness on the total reflectance and (b) reflectance from the selected thickness of 50 and 60 nm of front SnS layer.

Table 1 Photocurrent density of SnS Photoelectrodes in different systems

System	Light source (kW m^{-2})	Bias voltage (V vs. Ag/AgCl)	Photocurrent density (mA cm^{-2})	Reference
FTO-SnS(200 nm)-0.1M $K_4Fe(CN)_6$ + 0.01M $K_3Fe(CN)_6$	Sun simulator (1)	0.8	7	This study
FTO-SnS(500 nm)-0.1M $Na_2S_2O_3$	LED (0.3)	-1.2	0.7	36
FTO-SnS(600 nm) - 0.1M $K_4Fe(CN)_6$ + 0.01M $K_3Fe(CN)_6$	LED (0.6)	-0.15	1.1	27
FTO-Cu:SnS(600 nm)-0.1M $K_4Fe(CN)_6$ + 0.01M $K_3Fe(CN)_6$	LED (0.6)	-0.2	3.2	27
ITO-SnS(atomic layer)-0.5M Na_2SO_4	Sun simulator (1)	0.8	5.25	52
FTO-SnS(600 nm)-0.1M $Na_2S_2O_3$	LED (0.3)	0.6	0.1	46
FTO-SnS(20 nm)-$I^{3-/I-}$	Sun simulator (1)	0	0.087	53
ITO-SnS-TiO_2-0.5M Na_2S	Sun simulator (1)	0.042	1.55	54
FTO-SnS-$I^{3-/I-}$	Sun simulator (1)	0	0.07	55
ITO-SnS(monolayer)-0.1M Na_2SO_4	LED	0.8	6.5 × 10^{-6}	56
SnO_2-SnS(1-2 μm)-0.1M $FeCl_3$	Sun simulator (1)	0.042	0.65	57
FTO-SnS(1 μm)-0.1M $FeCl_3$	Sun simulator (1)	-0.358	0.25	58
Mo-SnS(500 nm)-0.1M H_2SO_4	Halogen (1)	-0.4	0.17	59
FTO-SnS(245 nm)-0.1M $Eu(NO_3)_3$	Sun simulator (1)	-0.65	0.17	29
Ti-Sb:SnS-0.1M $Na_2S_2O_3$	Xenon bulb (4.1)	-0.2	0.32	60

Table 2 Estimated fitting parameters of the equivalent circuit for photoelectrochemical cell made of nanostructured SnS electrode from the impedance spectroscopy for the applied potential 0.05-0.5 V vs. Ag/AgCl.

V_{App} (V vs. Ag/-AgCl)	Fitting parameters							Time constant	
	R_S (Ω)	R_J (Ω)	CPE-I		R_C (Ω)	CPE-II		t_j (ms)	t_c (ms)
			Q_J (μMho)	n_J		Q_C (μMho)	n_C		
0.05	53	3348.4	6.36	0.74	655.2	1.19	0.858	5.5	0.24
0.1	38.3	2989	4.19	0.786	1249.4	1.43	0.81	3.8	0.4
0.2	39.4	2042.5	4.21	0.825	1068.9	1.92	0.779	3.14	0.35
0.3	40.2	1191.9	4.36	0.826	864.6	2.05	0.774	1.72	0.28
0.4	31.4	79.4	22.1	1.01	1335.6	3.27	0.704	1.87	0.45
0.5	25.4	75.7	21.7	1.01	1380	2.39	0.715	1.75	0.34

Lewis and R. L. Brutchey, *Chem. Mater.*, 2014, **26**, 5444–5446.

30 P. Sinsermsuksakul, J. Heo, W. Noh, A. S. Hock and R. G. Gordon, *Adv. Energy Mater.*, 2011, **1**, 1116–1125.

31 H. Chandrasekhar, R. Humphreys, U. Zwick and M. Cardona, *Phys. Rev. B: Condens. Matter*, 1977, **15**, 2177.

32 L. Shi, Y. Xu and Q. Li, *Nanoscale*, 2010, **2**, 2104–2108.

33 A. Schneikart, H. Schimper, A. Klein and W. Jaegermann, *J. Phys. D: Appl. Phys.*, 2013, **46**, 305109.

34 J.-G. Kang, J.-G. Park and D.-W. Kim, *Electrochem. Commun.*, 2010, **12**, 307–310.

35 S. Zimin, E. Gorlachev, I. Amirov, V. Naumov, G. Dubov, V. Gremenok and S. Bashkirov, *Semicond. Sci. Technol.*, 2014, **29**, 015009.

36 M. Patel, I. Mukhopadhyay and A. Ray, *J. Alloys Compd.*, 2015, **619**, 458–463.

37 C. Honsberg and S. Bowden, *Double Layer Anti Reflection Coatings*, 2015, http://pveducation.org/pvcdrom/design/dlarc.

38 S. Chhajed, M. F. Schubert, J. K. Kim and E. Fred Schubert, *Appl. Phys. Lett.*, 2008, **93**, 251108.

39 J. Zhao and M. A. Green, *IEEE Trans. Electron Devices*, 1991, **38**, 1925–1934.

40 G. A. Tritsaris, B. D. Malone and E. Kaxiras, *J. Appl. Phys.*, 2014, **115**, 173702.

41 R. Armiento and A. E. Mattsson, *Phys. Rev. B: Condens. Matter*, 2005, **72**, 085108.

42 G. Kresse and J. Furthmüller, *Phys. Rev. B: Condens. Matter*, 1996, **54**, 11169.

43 G. Kresse and D. Joubert, *Phys. Rev. B: Condens. Matter*, 1999, **59**, 1758.

44 J. Vidal, S. Lany, M. dAvezac, A. Zunger, A. Zakutayev, J. Francis and J. Tate, *Appl. Phys. Lett.*, 2012, **100**, 032104–032104.

45 K. Gelderman, L. Lee and S. Donne, *J. Chem. Educ.*, 2007, **84**, 685.

46 M. Patel, I. Mukhopadhyay and A. Ray, *Opt. Mater.*, 2013, **35**, 1693–1699.

47 M. Patel and A. Ray, *ACS Appl. Mater. Interfaces*, 2014, **6**, 10099–10106.

48 D. B. Patel, K. R. Chauhan and I. Mukhopadhyay, *Phys. Chem. Chem. Phys.*, 2014, **16**, 20900–20908.

49 F. Fabregat-Santiago, G. Garcia-Belmonte, I. Mora-Seró and J. Bisquert, *Phys. Chem. Chem. Phys.*, 2011, **13**, 9083–9118.

50 S. Kumar, P. Singh and G. Chilana, *Sol. Energy Mater. Sol. Cells*, 2009, **93**, 1881–1884.

51 Y. Proskuryakov, K. Durose, B. Taele and S. Oelting, *Journal of Applied Physics*, 2007, **102**, 024504.

52 Y. Sun, Z. Sun, S. Gao, H. Cheng, Q. Liu, F. Lei, S. Wei and Y. Xie, *Adv. Energy Mater.*, 2014, **4**, 1–1.

53 J. Chao, Z. Wang, X. Xu, Q. Xiang, W. Song, G. Chen, J. Hu and D. Chen, *RSC Adv.*, 2013, **3**, 2746–2753.

54 Y. Jia, F. Yang, F. Cai, C. Cheng and Y. Zhao, *Electron. Mater. Lett.*, 2013, **9**, 287–291.

55 J. Chao, Z. Xie, X. Duan, Y. Dong, Z. Wang, J. Xu, B. Liang, B. Shan, J. Ye, D. Chen and G. Shen, *CrystEngComm*, 2012, **14**, 3163–3168.

56 S. G. Hickey, C. Waurisch, B. Rellinghaus and A. Eychmuller, *J. Am. Chem. Soc.*, 2008, **130**, 14978–14980.

57 B. Subramanian, C. Sanjeeviraja and M. Jayachandran, *Mater. Chem. Phys.*, 2001, **71**, 40–46.

58 B. Subramanian, C. Sanjeeviraja and M. Jayachandran, *Sol. Energy Mater. Sol. Cells*, 2003, **79**, 57–65.

59 N. Revathi, S. Bereznev, M. Loorits, J. Raudoja, J. Lehner, J. Gurevits, R. Traksmaa, V. Mikli, E. Mellikov and O. Volobujeva, *J. Vac. Sci. Technol., A*, 2014, **32**, 061506.

60 M. Seal, N. Singh, E. W. McFarland and J. Baltrusaitis, *J. Phys. Chem. C*, 2015, **119**, 6471–6480.